école normale supérieure paris—saclay
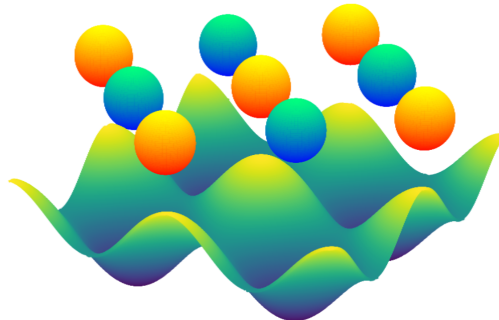
UNIVERSITEIT VAN AMSTERDAM

PREDOCTORAL YEAR OF RESEARCH ABROAD, FINAL REPORT

Alkali-alkaline earth mixtures in optical lattice potentials

Student:
Simon Lepleux
ENS Paris-Saclay
simon.lepleux@ens-paris-saclay.fr

Supervisors:
Prof. Dr. Florian Schreck
Dr. Klaasjan van Druten
Premjith Thekkeppatt

Strontium BEC group, Quantum Gases and Quantum Information group, Van der Waals-Zeeman Institute, Institute of Physics, Universiteit van Amsterdam

July 28, 2023

Contents

1 Introduction

In order to probe the fundamental laws of quantum mechanics, physicists have tried to cool down atoms and molecules to extremely low temperatures to observe them in their electronic, rotational or vibrational ground state. To this end, laser cooling technologies were developed such as the Zeeman slower [1], the magneto-optical trap [2] and the dipole trap [3]. Depending on the studied species, we make use of these three techniques in the lab to obtain ground state Bose-Einstein condensates (BEC) [4] or degenerate Fermi gases (DFG) [5]. At these temperatures it becomes possible to observe quantum phenomena such as matter-wave interferences [6] or quantum phase transitions [7], as well as to simulate complex condensed-matter phenomena [8].

Ultracold heteronuclear molecules have a richer internal structure than atoms and exhibit dipolar interactions. These exotic properties of ultracold molecules enable us to create and study few- and many-body quantum systems beyond the reach of atoms [9]. Until now, only ultracold gases of alkali dimer molecules have been realized and are being extensively studied [10]. Our goal in the RbSr experiment of the Strontium BEC group in Amsterdam is to create ultracold polar open-shell RbSr molecules in the rovibrational ground state. In contrast to alkali dimers, RbSr has three valence electrons, one of which is unpaired in the molecular ground state. This endows RbSr with a magnetic dipole moment in addition to the electric dipole moment exhibited by alkali dimers. These magnetic and electric dipole momenta are two handles with which we can control the molecules and create interesting few- and many-body systems. In previous experimental results from the team, Feshbach resonances were observed between bosonic ^{87}Rb and various isotopes of Sr [11]. These resonances are narrow due to the non-magnetic nature of Sr, but they should allow the creation of RbSr molecules by magneto-association [12].

In order to better understand the interactions playing a role in this alkali-alkaline earth mixture, we decided to work towards the creation of a new quantum system of ultracold Rb and Sr in an optical lattice potential [13]. If the wavelength of the light is chosen wisely, it is possible to generate a system where Rb and Sr respectively sit in the nodes and the anti-nodes of the periodic potential, thus reducing the inter-species spacing to a distance of only $\lambda/4$. At this scale, the inter-species interactions should be sufficient to observe changes in the single-species electronic band structure and tunneling properties. Furthermore, it should be possible to perform magneto-association of molecules using Feshbach resonances.

This report is organized as follows: I will first give insights into the theory of optical lattices and the behavior of atoms in these potentials, relying mainly on the results of my numerical simulation of an ultracold mixture of Rb and Sr in an optical lattice. I will then detail the design, construction, and characterization of a second harmonic generation (SHG) setup to generate $\lambda = 532$ nm light from a $\lambda = 1064$ nm narrow-linewidth laser source. I will conclude by giving an outlook on the future experiments that will be performed in extension to my work.

2 Rb and Sr mixture in an optical lattice potential

In this section, I am going to lay the theoretical basis required to understand the physics of ultracold atoms in optical potentials. Starting with the electric dipole force, I will derive the potential created by a retroreflected beam in 1, 2 and 3 dimensions. I will then study the ground state of an ultracold atomic cloud in such a potential and calculate the tunneling and interaction energy for single species. This will lead me to describe the quantum phase transition occurring for ultracold gases in deep optical lattices. I will finally describe the effects of inter-species interactions in a highly interacting system of Rb and Sr. All of the derivations will be illustrated by figures obtained by a numerical simulation that I realized with Python. The simulation can calculate the eigenvalues and eigenvectors of the Hamiltonian for a finite discrete system using the exact diagonalization algorithm [14].

2.1 Theory of optical lattices

2.1.1 The dipole force

When an atom is placed into laser light, the electric field $\mathbf{E}$ induces an atomic dipole moment $\mathbf{d}$ that oscillates at the driving frequency ω. The amplitude $\tilde{d}$ of the dipole moment is related to the field amplitude $\tilde{E}$ by $\tilde{d} = \alpha \tilde{E}$, where α is the scalar polarizability. We can then derive the interaction potential of the induced dipole moment as:

$$V_{dip} = -\frac{1}{2} < \mathbf{d} \cdot \mathbf{E} > = -\frac{1}{2\epsilon_0 c} Re(\alpha) I$$

With the field intensity $I = 2\epsilon_0 c |\mathbf{E}|^2$. If the atom can be accurately approximated by a two-level system, we can use Lorentz oscillator model [15] to describe the polarizability and obtain:

$$V_{dip}(\mathbf{r}) = -\frac{3\pi c^2}{2\omega_0^3} \left(\frac{\Gamma}{\omega_0 - \omega} + \frac{\Gamma}{\omega_0 + \omega} \right) I(\mathbf{r})$$

where ω_0 is the resonance frequency of the oscillator and Γ the spontaneous decay rate of the excited state. One can see that for positive values of the detuning $\Delta = \omega - \omega_0$ the interaction potential is positive (we say that the laser is "blue-detuned"). This will cause high-intensity regions of space to exert a repulsive force on the atom. However, for a negative detuning ("red-detuned" laser) the interaction energy is negative causing the atom to be attracted into high optical intensity regions.

2.1.2 Optical dipole potential

The intensity profile of a Gaussian beam in cylindrical coordinates is given by:

$$I(r, z) = \frac{2P}{\pi w^2(z)} \cdot e^{-\frac{2r^2}{w^2(z)}}$$

P is the total power of the laser light whereas $w(z) = w_0(1 + (z/z_r)^2)^{1/2}$ is the $1/e^2$ radius depending on the beam waist w_0 and the Rayleigh range $z_r = \pi w_0^2 / \lambda$. If we use a red-detuned laser beam, the atom will be attracted to the region with the highest optical

intensity: the center of the Gaussian beam. One can then trap neutral atoms or molecules inside the beam, creating an optical dipole trap [3]. Extremely focused dipole traps called optical tweezers can even be used to trap and manipulate single atoms or molecules [16].

2.1.3 Periodic lattice potential

The creation of periodic optical potentials is at the heart of quantum simulation because it allows physicists to simulate and study condensed-matter phenomena that can be challenging to observe in solids [8]. Because the spatial, spectral, and polarization properties of light can be extremely well controlled experimentally, a wide range of periodic potentials can be created and controlled with high precision: they are called optical lattices. The simplest form of optical lattice can be created by reflecting a Gaussian beam back onto itself in order to create a standing wave with a period of $\lambda_{lat} = \lambda/2$. This configuration is represented in figure 1 taken from [17].
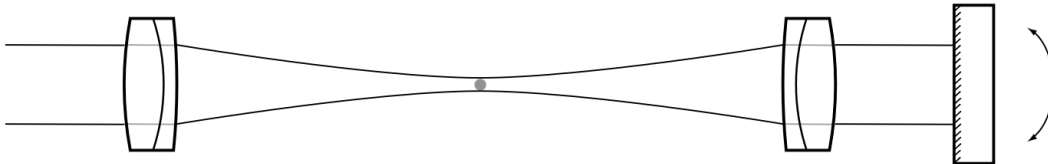

Figure 1: Optical lattice generated by a retroreflected Gaussian beam.

In the center of the beam where $z < z_r$, the trapping potential of a 1D lattice can be expressed as:

$$V(r,z) = -V_{lat} \cdot e^{\frac{-2r^2}{w_0^2}} \cdot sin^2(kz) \simeq -V_{lat} \cdot \left(1 - \frac{2r^2}{w_0^2}\right) \cdot sin^2(kz)$$

where V_{lat} is the lattice dept and $k = \frac{2\pi}{\lambda}$ is the amplitude of the wavevector of the light. In this configuration, constructive interference doubles the amplitude of the electric field compared to a simple Gaussian beam, the intensity is therefore multiplied by 4. It is convenient to specify the lattice depth in terms of the recoil energy E_r: the kinetic energy gained by one atom after absorbing or emitting a photon in the lattice beam. It can be expressed as $E_r = \frac{\hbar^2 k^2}{2m}$ where m is the mass of a single atom. For this 1D lattice, we can derive the radial trapping frequency $\omega_r^2 = \frac{4V_{lat}}{mw_0^2}$ and the axial trapping frequency $\omega_{lat}^2 = 2V_{lat}k^2/m$. The number of lattice sites in the center of the beam can be easily approximated by $N = 2z_r/\lambda_{lat} = 4z_r/\lambda$. However, we need to take into account that atoms at nanokelvin temperature do not have enough energy to tunnel across the whole Rayleigh range, thus reducing the number of occupied sites.

We can observe that for $\lambda << w_0$ (typically true for lattice beams), the radial confinement induced by the Gaussian intensity distribution is weak compared to the axial confinement due to the interference pattern. This results in the pancake-shaped traps visible in figure 2(a). Their shape differs fundamentally from the confinement experienced by electrons in traditional solids but can be used to study interactions between close layers of atomic gases. In order to generate optical lattices of higher dimensionality, we can
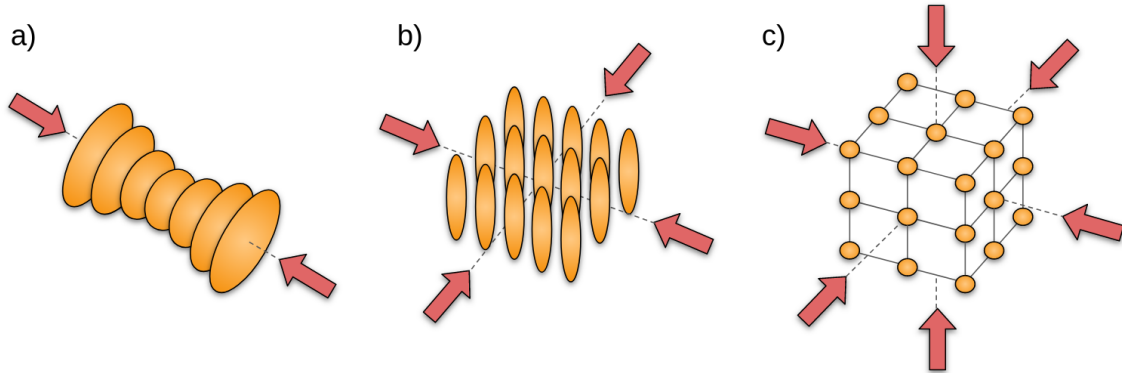
Figure 2: Structure of the optical lattice for 1 (a), 2 (b), and 3 (c) retroreflected beams. Some sites are hidden on (c) for clarity purposes.

superimpose standing waves from different orthogonal directions. As represented in figure 2(b) and (c), a 2D lattice potential is composed of a 2D grid of cigar-shaped traps while a 3D lattice potential will resemble a real crystalline cubic lattice. To generate accurately these patterns, we make sure that the polarizations of each beam are mutually orthogonal and that their frequency is slightly shifted by a few tens of MHz. This has the effect of destroying every residual interference between the different standing waves.

2.2   Atomic gases in an optical lattice

The strength of optical lattices resides in their tunability. With clever manipulation of the frequency or polarization of the light, the simulation of any form of periodic potential with extreme precision becomes achievable. Possibilities can range from triangular lattices to the Kagome lattice, intensively studied in condensed matter physics [18].

A second handle for tunability resides in the possibility to load different atoms and molecules inside these optical lattices. Choosing to load bosonic or fermionic species in a lattice can lead to the formation of Bose-Einstein condensates [4] or degenerate Fermi gases [5]. Van der Waals interactions can be studied by loading neutral atoms in optical lattices, while molecules or highly dipolar atoms like Erbium be used to probe the long-range and anisotropic dipole-dipole interaction [19]. Controlling the lattice potential can even allow the manipulation of atomic interactions like in confinement-induced resonances [20].

In this section, I chose to describe the physical properties of neutral atoms and molecules inside a 1D optical lattice potential. This description serves as a basis for the study of the quantum system studied in section 2.3.

2.2.1   Band structure and Bloch functions

The movement of atoms and molecules in a periodic potential is described by the apparition of a band structure [21]. The system of one particle in a periodic potential can be fully described by the Hamiltonian $\hat{H}(q, V_{lat})$ depending on the lattice depth and the quasi-momentum $q \in [-\hbar \cdot k_{lat}/2, \hbar \cdot k_{lat}/2]$. For a 1D sinusoidal potential, the Hamiltonian is

defined as:

$$\hat{H}_{l,l'} = \begin{cases} \frac{(q+l\cdot k_{lat}))^2}{2m} & \text{if } l = l' \\ -V_{lat}/4 & \text{if } |l-l'| = 1 \\ 0 & \text{else} \end{cases}$$

where l and l' $\in [-\frac{N}{2}, \frac{N}{2}]$ with N the number of lattice sites. I developed a simulation that performs the exact diagonalization of $\hat{H}$ and derives its eigenenergies and eigenfunctions [14]. These values are denoted by the number (n), the band index. We can then observe the band structure by plotting the eigenvalues $E^{(n)}(q)$ for each value of the quasi-momentum q.
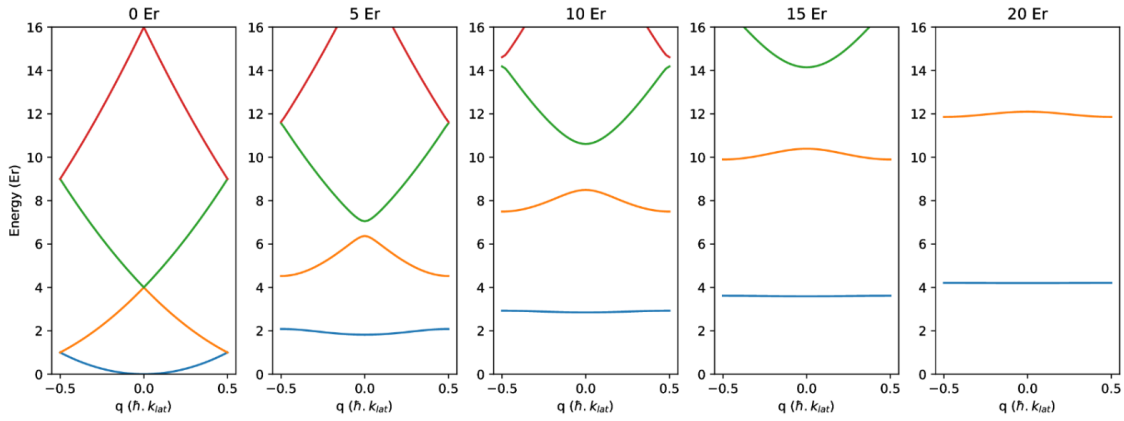

Figure 3: Evolution of the 4 lowest energy bands of a 1D lattice when the lattice depth is increased.

Figure 3 shows the evolution of the band structure for increasing values of V_{lat}. We can see that for $V_{lat} = 0 \, E_r$ there is no bandgap and the energy spectrum of a particle in the lattice corresponds to the one of a plane wave. When the lattice depth increases, the bandgap increases, and the energy spectrum shifts to the one of a harmonic oscillator with frequency $\omega = \omega_{lat}$. This behavior can be explained by the fact that atoms in a very deep sinusoidal trap will only experience the harmonic part of the potential. Indeed, their low thermal energy compared to the trap depth forbids them to explore higher energy levels.

We can see a clearer form of this phenomenon if we study the eigenfunctions of $\hat{H}$. They are solutions to the Schrödinger equation and can be expressed from Bloch's theorem as:

$$\phi_q^{(n)}(x) = e^{iqx/\hbar} \cdot u_q^{(n)}(x)$$

with $u_q^{(n)}(x)$ having the same periodicity as the lattice potential. These eigenfunctions are called Bloch functions and they are calculated by the simulation for the first band at different values of q. They are plotted in figure 4(a). We can see that the wavefunctions show a periodic behavior modulated by a plane wave of momentum q. If the lattice depth is increased, the probability density $|\phi|^2$ peaks on the position of the lattice sites and vanishes between them. This behavior explains the phenomenon observed in figure 3: for deep lattices, the probability density is bigger in the center of the sites where the potential can be expressed as a harmonic potential.
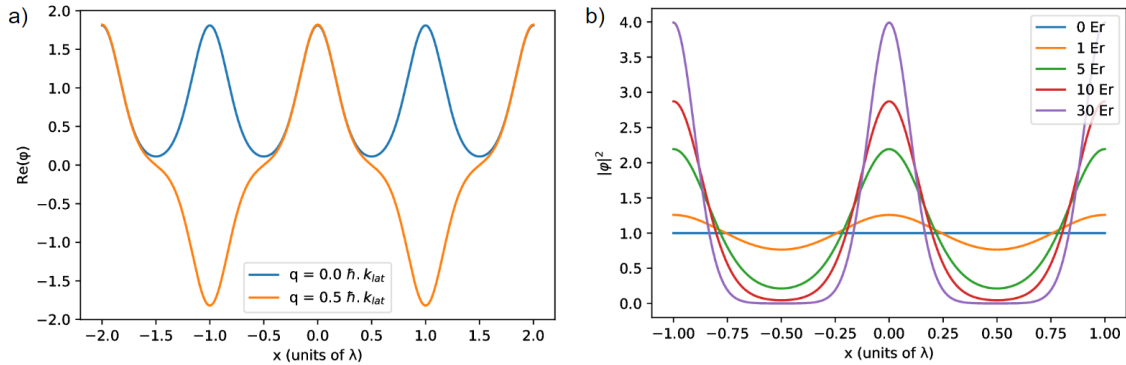
Figure 4: (a) Real part of Bloch functions for different quasi-momentum (b) Modulus of Bloch functions for different lattice depths.

2.2.2   Wannier functions

The fact that Bloch functions are delocalized over the whole lattice implies that they fail to describe the probability density of strongly localized atoms in deep optical lattices. Here we consider a deep lattice for values of V_{lat} higher than few E_r where the first band is almost flat. To describe these cases, we make use of Wannier functions [22]. They constitute an orthogonal basis of wavefunctions that are normalized and maximally localized to individual lattice sites. They can be derived from Bloch functions through the transformation:

$$w^{(n)}(x - x_i) = \frac{1}{\sqrt{\mathcal{N}}} \sum_q e^{-iqx_i/\hbar} \cdot \phi_q^{(n)}(x)$$

with x_i the position of the ith lattice site and $\mathcal{N}$ a normalization constant. It can be proven easily that the Wannier function at the site x_{i+1} is simply the function $w_i(x)$ translated by λ_{lat}. We can then simplify our study of these functions to the one localized in the 0th site. Due to the low energy of ultracold atoms in our system, we can also limit ourselves to the study of Wannier functions of the first band. Unless specified, all the Wannier functions studied from now on will be from the first band and the superscript $^{(1)}$ will be omitted.

A representation of the probability densities of Wannier functions on 3 neighboring sites is visible in figure 5(a). We can see that the Wannier function w_i has a peak at the site x_i and smaller sidelobes appears on both edges. For all Wannier functions, the probability density shows an exponential decrease with $|x - x_i|$. When the lattice depth is increased, Wannier functions will exhibit a stronger peak at their center as shown in figure 5(b). At the same time, the amplitude of the sidelobes decreases, thus increasing the localization of the atom. Thanks to their localized and normalized nature, Wannier functions allow not only to describe the dynamics of atoms and molecules in deep optical lattices but also to build a bridge to a well-known description of particles in periodic potentials: the Hubbard model [23].
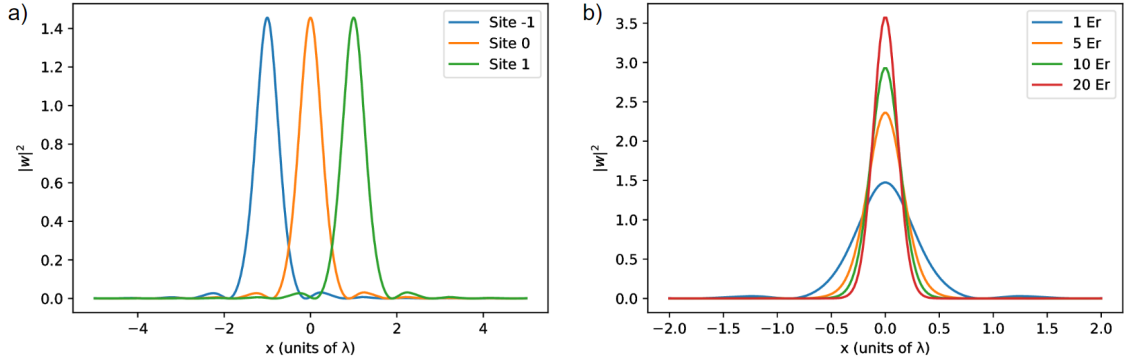
Figure 5: (a) Modulus of Wannier functions on different lattice sites (b) Modulus of Wannier functions for different lattice depths.

2.2.3 Bose-Hubbard Hamiltonian

At this stage, the simulation only accounts for one particle inside the periodic potential. In order to study the quantum gas of Rb and Sr in an optical lattice, we need a theory to describe intra- and inter-species interactions. The simplest and most efficient model to describe particles in a periodic potential is the Hubbard model [23]. Indeed, as electrons in a solid described by the Fermi-Hubbard model, bosonic atoms inside an optical lattice can be described accurately by the Bose-Hubbard Hamiltonian:

$$\hat{H} = -J \sum_i \left(\hat{b}_i^\dagger \hat{b}_{i+1} + \hat{b}_{i+1}^\dagger \hat{b}_i \right) + \frac{U}{2} \sum_i \hat{n}_i (\hat{n}_i - 1)$$

where $\hat{b}_i^\dagger$, $\hat{b}_i$ and $\hat{n}_i = \hat{b}_i^\dagger \hat{b}_i$ are the creation, annihilation and density operators on the ith site. We can interpret $\hat{b}_i^\dagger$ and $\hat{b}_i$ as operators that create or annihilate a particle in the Wannier state $|w_i\rangle$ described by the Wannier function w_i. For now, this Hamiltonian only describes the dynamics of one atomic species in an optical lattice, we will extend the study to describe a mixture of two species in section 2.3.

The Bose-Hubbard Hamiltonian is defined solely by the tunneling energy J and the on-site interaction energy U. These parameters are crucial to the study of the dynamics of a simple quantum system. They can be derived from the band structure and the Wannier functions studied previously. We know by [24] that the tunneling energy can be approximated by:

$$J \simeq \frac{max(E^{(0)}(q)) - min(E^{(0)}(q))}{4}$$

Whereas the on-site interaction energy can be derived from the atomic wavefunction $\Psi(\mathbf{x})$ by:

$$U = \frac{4\pi \hbar^2 a}{m} \int d^3 \mathbf{x} \, |\Psi(\mathbf{x})|^4$$

where a is the inter-species scattering length of the atoms. $\Psi(\mathbf{x})$ is a 3D wavefunction and has different definition for atoms in 1D, 2D or 3D lattices.

2.2.4 3D wavefunction

In order to obtain the on-site interaction (and later on the inter-species interaction), the 3D wavefunction has to be calculated. Because lattice beams do not interfere with each other in our study, we can express Ψ as a product of 1D wavefunctions:

$$\Psi(\mathbf{x}) = \begin{cases} w_x(x) \cdot w_y(y) \cdot w_z(z) & \text{for a 3D lattice} \\ w_x(x) \cdot w_y(y) \cdot \Theta_z(z) & \text{for a 2D lattice} \\ w_x(x) \cdot \Theta_y(y) \cdot \Theta_z(z) & \text{for a 1D lattice} \end{cases}$$

with Θ_i the ground state wavefunction of the atom in a Gaussian potential on the i axis. In the following calculations, the low atomic temperature allows us to approximate the radial Gaussian trap by a harmonic potential as shown in section 2.1.3. As it can be delicate to obtain a mental picture for a 3D function, I used the simulation to plot it.
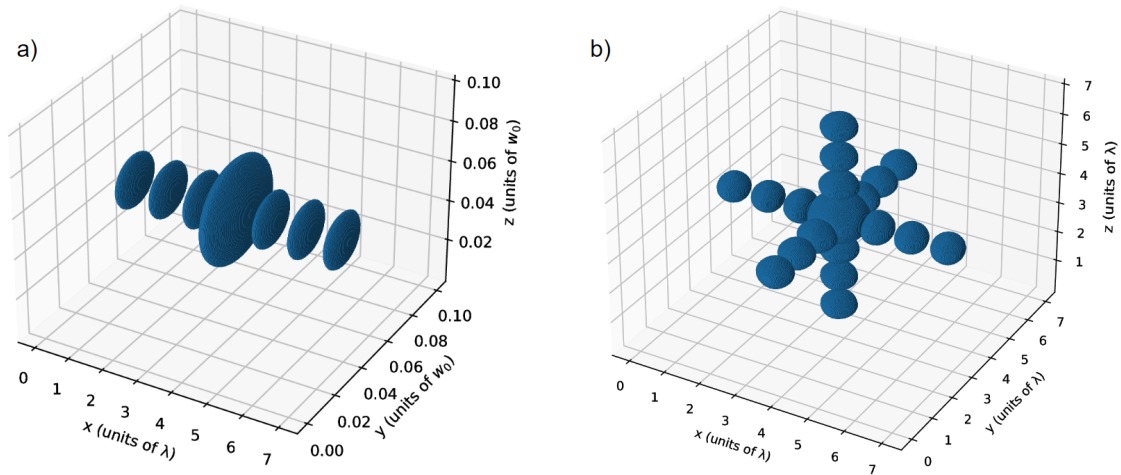

Figure 6: Probability density for the position of a Sr atom in a 1D (a) and a 3D (b) optical lattice.

Figure 6(a) shows a 3D representation of $|\Psi(\mathbf{x})|^2$ in the case of a Sr atom in a 1D lattice oriented in the $\vec{x}$ direction. We can see that the atom is mostly localized in a pancake-shaped central lobe positioned onto a lattice site. We also notice the apparition of smaller sidelobes in the $\vec{x}$ direction resulting from the extension of the shape of the Wannier function $w(x - x_i)$ in 3 dimensions. These lobes are responsible for the tunneling of atoms from one site to another. The probability density of the same atom inside a 3D lattice is shown in figure 6(b). In this case, strong confinement is experienced in every direction. This results in a spherical central lobe and smaller spherical sidelobes expanding in the direction of the 3 lattice beams.

2.2.5 Quantum phase transition

Using the deviations from section 2.2.3, we can use the simulation to compute the evolution of J and U with increasing lattice depth. Figure 7(a) shows that tunneling energy in deep lattices reduces exponentially. This behavior is associated with the reduction of the

amplitude of the sidelobes in the atomic wavefunction observed in section 2.2.2. Figure 7(b) shows the simulation results for the on-site energy calculation of Sr atoms in a 3D lattice. We observe an increasing interaction energy for deeper lattices due to the stronger localization of atoms in lattice sites. These results are compared to the theoretical on-site energy for atoms in the ground state of a harmonic oscillator. The slight mismatch between theoretical and simulated values can be explained by the simulation using real Wannier functions to describe the atom instead of approximated Gaussian wavefunctions.
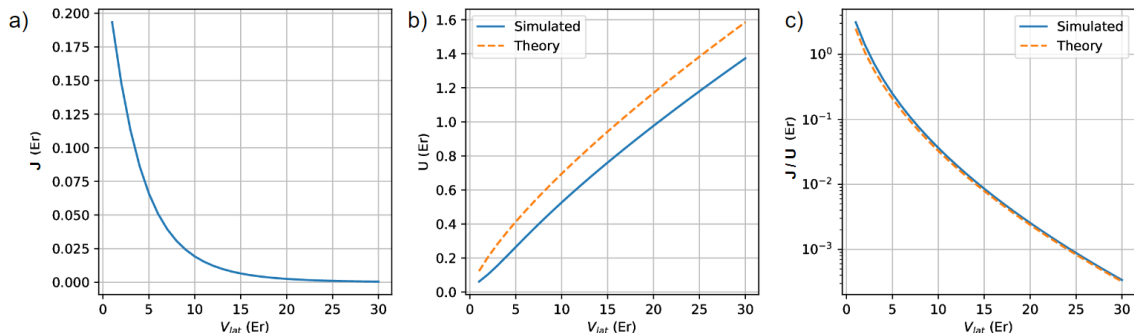

Figure 7: (a) Tunneling energy with increasing lattice depth, (b) Evolution of the on-site interaction energy with increasing lattice depth for a 3D lattice (blue) compared to theoretical expression (orange dotted line), (c) J/U ratio with increasing lattice depth (blue) compared to the theoretical values (orange dotted line).

Figure 7(c) shows the evolution of the ratio J/U for different lattice depths compared to theoretical values for atoms in a harmonic oscillator ground state. The simulation demonstrates very good agreement with the theory. This ratio is a crucial quantity when studying ultracold atoms in optical lattices because it carries information about the balance between kinetic and potential energy in the system. We know from [7] that for large lattice depths, the exponential suppression of tunneling and the increase of interaction energy leads the ultracold system to enter a strongly correlated regime. This phenomenon is described as a quantum phase transition from a superfluid state to a Mott insulator state and occurs for a critical value of the J/U ratio. The transition was first developed to explain the dynamics of strongly correlated electrons in a solid [25], but was subsequently observed for atomic gases in an optical lattice potential. In the literature, we observe the phase transition inside a 3D lattice for values of J/U around 10^{-2}, corresponding to lattice depths of around 16 Er [7]. This value matches with the simulated value of 15 Er observed in figure 7(c).

After reaching the critical value of J/U, the ultracold quantum system behaves differently from a non-interacting Bose gas. Atoms that previously tend to delocalize over the whole lattice find themselves strongly localized on lattice sites. Long-range interactions disappear and nearest-neighbor interactions start to dominate. The time scale of this transition is on the order of the tunneling time $\tau = \hbar/J$.

Figure 8 taken from [17] shows the result of a typical atom number measurement on a 2D optical lattice. For a superfluid state represented in figure 8(a), the delocalized atoms appear randomly over the whole lattice following a Poisson distribution. This distribution is governed by the average occupation number $\bar{n}$ defined as $\bar{n} = N_{atoms}/N_{sites}$. In an
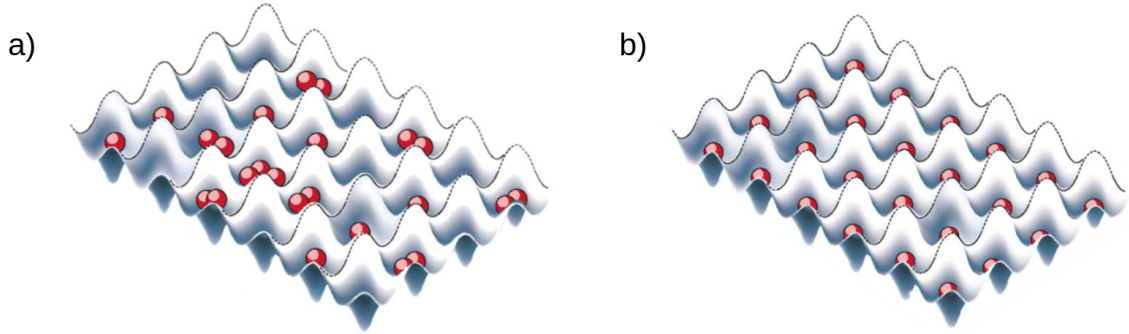
Figure 8: Result for the measurement of atom number in a 2D optical lattice for a super-fluid state (a) and a Mott insulator state (b).

opposite manner, atoms in a Mott insulator state distribute homogeneously across the whole lattice to reduce the total interaction energy of the system as shown in figure 8(b). The number of atoms in each site is then equal to $\bar{n}$. The homogeneous nature and high interactions present in the Mott insulator state make it an optimal system to perform quantum simulation or to study interactions between the trapped particles.

2.3   Interactions between Rb and Sr in an optical lattice

Previous results obtained on the RbSr experiment led to significant progress towards the creation of ultracold polar open-shell RbSr molecules in the rovibrational ground state. Important investigations were made on the properties of the ground state of the RbSr molecule [26] and Feshbach resonances were observed between [87]Rb and [87]Sr [11]. More-over, this isotopic combination exhibits a high inter-species scattering length measured to be around 1500 a_0, where a_0 is the Bohr radius. We now need to expand our knowledge of the interactions between these two species. As the Van der Waals interactions between neutral atoms scale as $1/r^6$ with the interatomic distance r, it is necessary to bring these atoms closer to each other to enhance the interaction strength. However, shortening the interatomic distance too much is not a solution because it would heat the sample and increase the rate of 3-body collisions in a bulk sample [27].

From this consideration came the idea to study a mixture of [87]Rb and [87]Sr in a deep optical lattice at $\lambda = 532$ nm. Indeed, the main transition of Sr at $\lambda = 461$ nm makes the trapping of Sr atoms in such a red-detuned optical lattice possible, as seen in section 2.1.1. On the other hand, the D1 and D2 transitions of Rb respectively at $\lambda = 780$ nm and $\lambda = 795$ nm ensures that Rb atoms will experience a repulsive force from the intensity nodes of this same lattice and sit in the antinodes. If we overlap a dipole trap on top of the lattice to tightly confine both species, we can create a new quantum many-body system of strongly interacting Rb and Sr.

Figure 9 shows a representation of the quantum system where Sr and Rb occupy respectively the nodes and the antinodes of a 1D green lattice at $\lambda = 532$ nm. From this configuration, we observe that the spacing between the two species is reduced to $\lambda/4 = 133$ nm thus greatly increasing the inter-species interaction while at the same time reducing heating and 3-body collisions.
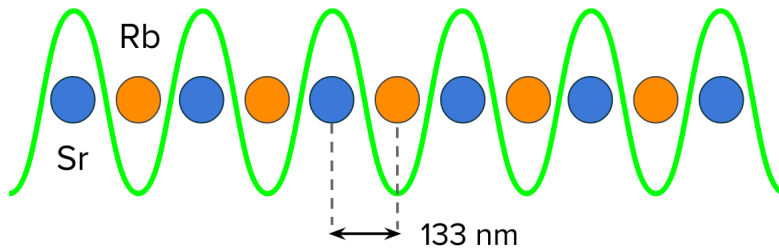
Figure 9: Mixture of Rb and Sr in an optical lattice at $\lambda = 532$ nm.

2.3.1   Inter-species interaction energy

We can refer to section 2.2.4 to derive the 3D wavefunction of Rb and Sr in the 1D green lattice. Figure 10(a) shows the overlap of the probability densities for the position of Sr (blue) and Rb (orange) atoms separated by $\lambda/4$ nm. We can see that the Rb wavefunction appears to be slightly bigger than the Sr wavefunction. This is due to the fact that Rb experiences a smaller lattice depth at this wavelength, as demonstrated in section 2.1.1. Sr atoms are therefore more strongly localized on the lattice sites than Rb atoms.
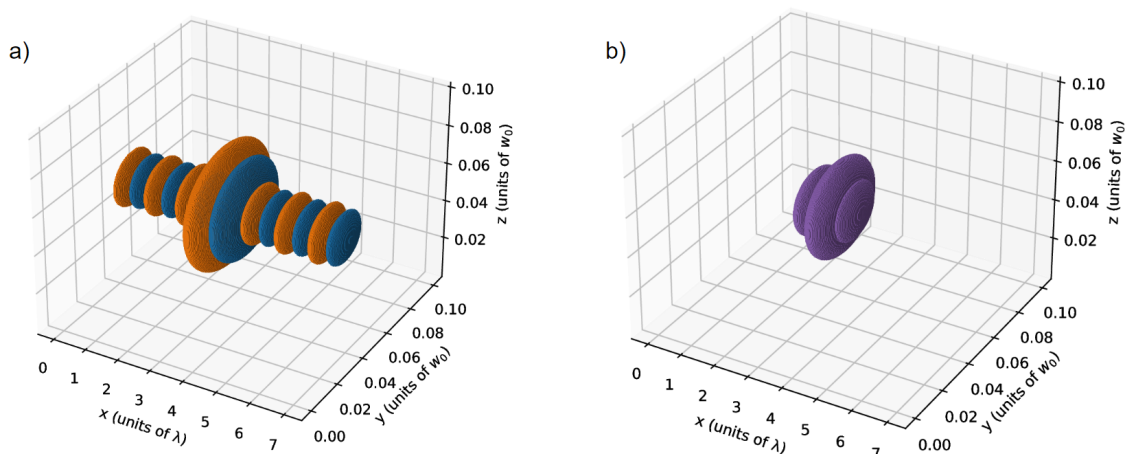

Figure 10: (a) Overlap of the wavefunctions of a Strontium atom in a lattice site (blue) and a Rubidium atom in the neighboring lattice antinode (orange) for a 1D lattice. Distances are given in units of wavelength (and beam waist) in the direction of strong (and weak) confinement, (b) Shape of the wavefunction resulting from the product of the two atomic wavefunctions.

We can then express the inter-species interaction between one atom of each species U_{RbSr} in the same fashion as the calculations from section 2.2.3. Indeed, the Bose-Hubbard model is still valid to study the system of bosonic ^{87}Rb and fermionic ^{87}Sr because of the lack of fermionic repulsion between these two species. We then have:

$$U_{RbSr} = \frac{4\pi\hbar^2 a_{RbSr}}{m} \int d^3\mathbf{x}\, |\Psi_{Rb}(\mathbf{x})|^2 \cdot |\Psi_{Sr}(\mathbf{x})|^2$$

where a_{RbSr} is the inter-species scattering length, Ψ_{Rb} is the wavefunction associated with the Rb atom in an antinode of the lattice, and Ψ_{Sr} describes a Sr atom in the neighboring lattice site. The shape of the product of the wavefunctions is shown in figure 10(b). We can see that only one central lobe and two non-symmetric sidelobes are visible, showing that most of the interaction occurs between the two central lobes of the atomic wavefunctions.

The calculation of U_{RbSr} is done in the case where there are only two atoms in the lattice. In order to extend the calculation to match the actual quantum system, the interaction energy for two atoms has to be multiplied by the average number of atoms in each lattice site $\bar{n}$. Also, to consider the interaction with all of the near neighbors we have to multiply U_{RbSr} by the coordination number of the lattice c, being respectively 2, 4 and 8 for 1D, 2D and 3D lattices. We can then express the total inter-species interaction energy as $U_{Tot} = c \cdot \bar{n} \cdot U_{RbSr}$. The calculation of U_{Tot} for different lattice depths is shown in figure 11(a). We plot U_{Tot} with respect to the lattice depth for Rb because it is the less deeply trapped species. We can see that the interaction energy decreases for higher lattice depths due to the stronger localization of atoms in their respective sites. The error bars represent the uncertainty on the average number of atoms per site $\bar{n}$ that can easily vary experimentally. We see that the overall strength of the interaction is around 4 kHz for a lattice depth of 15 Er. This strength is sufficient to allow the measurement of the interaction with the microwave clock spectroscopy setup already implemented in the RbSr experiment.
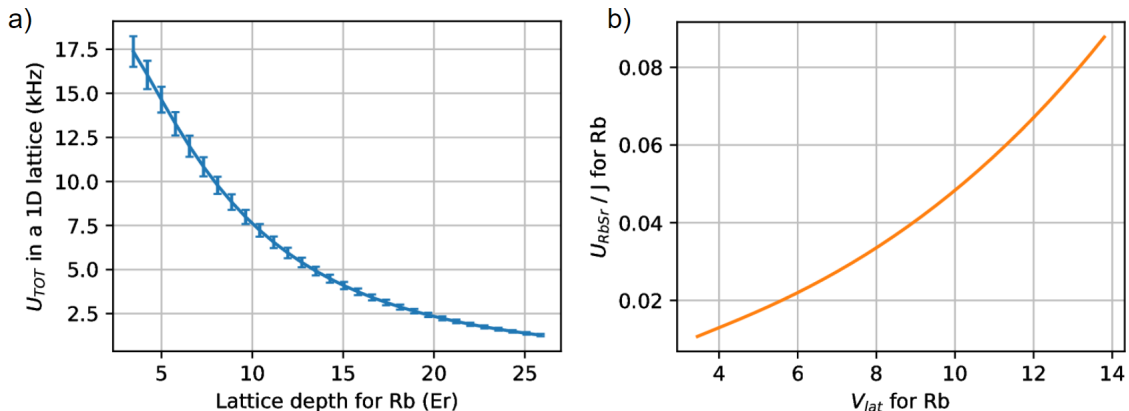

Figure 11: (a) Total interaction energy between Rb and Sr for different lattice depths, (b) Evolution of the U_{RbSr}/J ratio for Rb when the lattice depth is increased

Figure 11(b) shows the evolution of the ratio U_{RbSr}/J for Rb when the lattice depth is increased. Even though the inter-species interaction energy reduces with increasing lattice depth, the ratio U_{RbSr}/J increases, proving that the interaction energy decreases at a slower pace than the tunneling energy. This observation demonstrates that the presence of Sr atoms in the lattice enhances the localization of Rb atoms and leads to the creation of a strongly correlated system.

The results obtained in this section justify the use of an optical lattice at $\lambda = 532$ nm to increase the interaction between Rb and Sr, and they motivate the construction and experimental study of this quantum system.

2.4 Further developments of the simulation

Even though the simulation allowed me to estimate the interaction between Rb and Sr atoms in a $\lambda = 532$ nm lattice, a lot of improvements could still be implemented. First of all, the simulation could be extended to calculate the inter-species interaction energy in 2D or 3D. These results would be very helpful in the near future when the RbSr experiment will include a 2D or 3D green lattice.

Also, approximations were made on the calculation of atomic wavefunctions in 1D lattices. On the axis of weak confinement, the thermal energy of the atoms can exceed the spacing between the different excitation levels. This can lead the atomic wavefunction to spread on distances way larger than the size of the Gaussian ground state considered in this work.

The simulation could also be upgraded to take into account the external confinement of the lattice potential due to the Gaussian shape of the lattice beam or the presence of additional dipole traps. Indeed, out of the center of a Gaussian beam the intensity decreases rapidly, reducing the effective depth of the lattice. However, the lattice considered in the present simulation is perfectly sinusoidal in the axis of strong confinement. This leads to different tunneling dynamics and can affect the quantum phase transition from a superfluid to a Mott insulator. Taking into account the external confinement would also allow us to simulate the typical "wedding-cake" structure observed during the quantum phase transition [7].

Overall, a lot of interesting physical phenomena could be probed with simple adjustments to the simulation. We could for instance study how an increasing number of Rb atoms between the lattice sites impacts the tunneling rate of Sr atoms. We could also take into account the magnetic properties of Rb and try to calculate the strength of the Feshbach resonances observed by the group between these two species, but this time in a new quantum system [11].

3   Generation of the lattice light

This section mainly focuses on the generation of the $\lambda = 532$ nm light necessary to study the quantum system described in section 2.3. I will first go through the design of a second harmonic generation (SHG) setup to generate $\lambda = 532$ nm light from a $\lambda = 1064$ nm narrow-linewidth laser source. I will then detail my work on the design of custom thermal isolation parts. I will finish by characterizing the performances of the setup.

3.1   Installation of a high power laser

Future plans for the RbSr experiment include the realization of a 3D superlattice constituted of two superimposed 3D lattices at 1064 nm and 532 nm [28]. To this end, the optical power needs to be distributed from a single high-power narrow-linewidth laser to all of the 6 future beams of the lattice. We decided to build an optical setup that would allow the distribution of the infrared (IR) light at $\lambda = 1064$ nm generated by a COHERENT Mephisto MOPA 42W laser among several different output optical fibers. We chose to use this commercial-grade laser because it was already owned by the group but was currently unused. It exhibits a spectral linewidth below 3 kHz and relative intensity noise below -130 dB/Hz thus making it adequate for second harmonic generation and optical lattice generation. In order to watercool the laser, a chiller circuit with 60 l/min of water at 25°C was installed. I built an interlock system with an ARDUINO UNO microcontroller that turns off the laser if the flow signal measured by a flowmeter drops below 50 l/min.
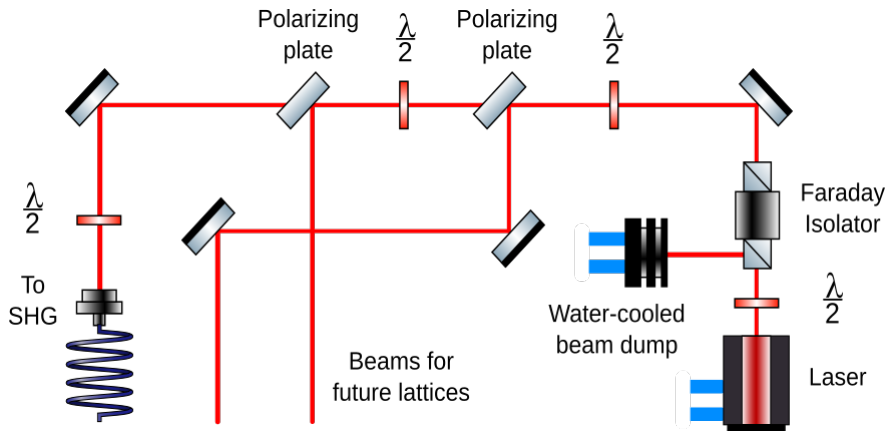

Figure 12: Optical power distribution setup

Figure 12 shows the optical layout of the power distribution. An adjustable amount of the laser light is first sent to a homemade water-cooled beam dump thanks to a $\lambda/2$ waveplate. This allows to change the out-coupled optical power while letting the laser operate at its optimal parameters. The remaining light is then sent through a Faraday isolator with 30 dB isolation protecting the source from any back-reflected light. Two sets of $\lambda/2$ waveplates and polarizing beamsplitter plates are then used to divide the optical path into 3 different ones with adjustable power. We decided to use beamsplitter plates instead of regular beamsplitter cubes due to the extraordinarily high damage threshold of the plates. These 3 final beams can then be coupled into optical fibers or divided

further for any other uses. Half-wave plates allow us to align the polarization of the light to the slow or fast axis of the polarization-maintaining fiber. The whole setup fits on a stand-alone 60x60 cm breadboard allowing for easy transportation.
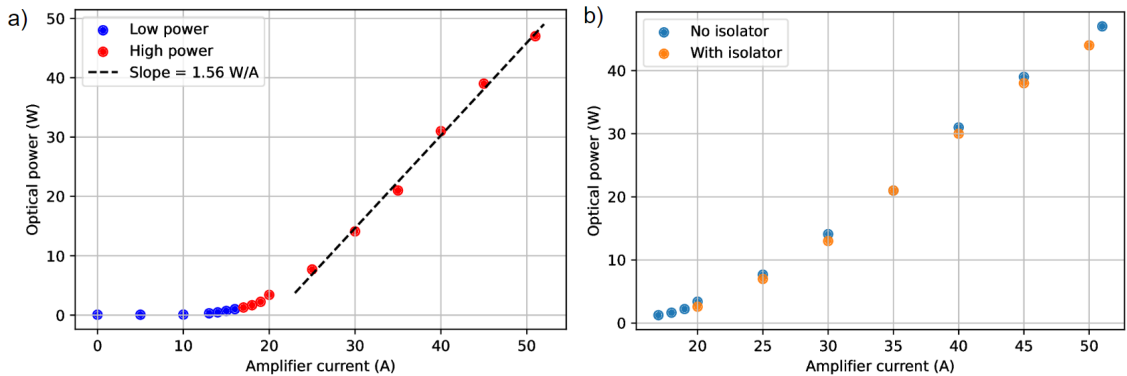

Figure 13: (a) Optical power of the Mephisto for different amplifier currents, (b) Optical power after and before the optical isolator.

The performances of the laser were characterized using a calibrated high-power power-meter. Figure 13(a) shows a measurement of the output optical power with respect to the current sent through the integrated amplifier of the laser. We can see that the laser power is firstly not increasing and then reaches a threshold value at around 20 A. The optical power then follows a linear slope of 1.56 W/A until it reaches its maximum at 47 W, a value higher than the 42 W specified by the manufacturer. After transmission through the Faraday isolator, the same measurement was performed and yielded a transmission factor of 96% as shown in figure 13(b). We would usually expect transmission and isolation values around 85 % and 40 dB for a Faraday isolator, so it is possible that I obtain such a high transmission at the price of a relatively low isolation power.

3.2 Design of the second harmonic generation setup

Many methods are available to perform the second harmonic generation (SHG) of laser light. The most common ones are intra-cavity doubling with nonlinear crystals such as lithium triborate (LBO), β-barium borate (BBO), or potassium titanyl phosphate (KTP) [29]. In these methods, the crystal is placed inside an optical cavity and multiple passages of the light through the crystal allow to increase the SHG efficiency. In 1962, the quasi-phase-matching technique was developed [30]. In this technique, the nonlinear crystal is periodically poled using a wide range of techniques. Pulsed electric field, electron bombardment, thermal pulsing, or other methods can be used to reposition the atoms in the lattice, creating oriented domains [31]. The phase mismatch that would normally accumulate over the crystal due to the lack of phase-matching is now compensated by the crystal's periodicity. We can then obtain extremely high SHG efficiency with only one single passage through the crystal. On top of that it allows to get rid of the use of a cavity, thus greatly simplifying the alignment.

For this reason, we chose to use a magnesium-oxide-doped periodically poled lithium niobiate (MgO:PPLN) crystal from the COVESION company to realize high-efficiency

single pass SHG generation of $\lambda = 532$ nm light from a $\lambda = 1064$ nm source. This crystal is 40 mm long and has an effective nonlinear coefficient d_{eff} of 14 pm/V (to compare to the usual 3.4 pm/V of KTP). It contains 5 different waveguides with poling periods ranging from 6.48 µm to 6.62 µm. To obtain the following results, I used the 6.59 µm poling period that allows phase-matching at a temperature around 214 °C.
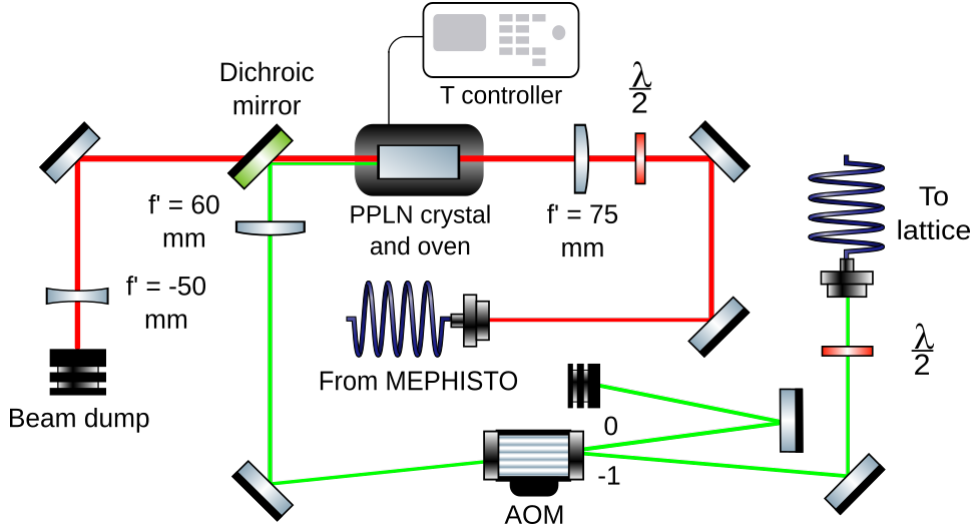

Figure 14: Second harmonic generation setup

The optical setup is presented in figure 14. I first had to verify that the polarization of the input IR light from the Mephisto was not affected by the two dielectric mirrors. I measured the circularity of the polarization to be 0.3 % before the mirrors and 0.4 % after, proving that the effect was negligible. Given that, I adjusted the polarization of the input light with a half-wave plate to the axis of the crystal that yields the best nonlinear coefficient. The beam is then focused through the crystal's waveguide with a $f' = 75$ mm lens. The crystal itself is mounted in a commercial oven from COVESION that allows the temperature to be stabilized with 10 mK precision with a PID controller. A dichroic mirror splits the IR light and the freshly generated green light. Approximately 99 % of the green light is reflected, and 95 % of the IR light is transmitted. The IR light is diverged into a beam dump by an $f' = -50$ mm lens to avoid excessive heating while the green beam is collimated by an $f' = 60$ mm lens. I then used an acousto-optic modulator (AOM) to reduce the intensity fluctuations of the beam. Indeed, by modulating the intensity of the sound wave in the AOM, one can control the intensity of the first-order diffracted beam. This will be useful to compensate for intensity fluctuations of the green beam and obtain a stable lattice. The beam is finally sent through a polarization-maintaining fiber to generate the future lattice.

3.2.1   Design of custom thermal isolation parts

Many parts of the SHG setup are subject to very high temperatures. The internal temperature of the oven itself reaches 214 °C and can heat the surrounding materials. This can cause convection and variations in the refractive index of air and thus destroy the

phase stability of the laser beam resulting in an unstable optical lattice. Also, the optical fibers are subject to heating due to the intense beams focused on the fiber tip by the fiber collimator. We observed that these commercial air-gap high-power fibers can reach temperatures above 70 °C when exposed to 10 W of optical power. At these temperatures, thermal instabilities can translate into mechanical instability of the fiber tip causing it to move or even oscillate, thus drastically decreasing the coupling efficiency.

For these reasons, we decided to build custom parts to improve the thermal isolation and stabilization of the hot elements. For each of these designs, I would first draw the piece on the computer-aided design software AutoCAD INVENTOR and place it in a drawing of the whole SHG setup. This allowed me to plan for dimensioning, assembly and mounting solutions of each part in the final experiment. I worked with the Technical Center of the University of Amsterdam to build these parts using water-jet cutting machines and milling machines. In order to test the performances of the designs, I used a commercial infrared camera from TELEDYNE FLIR to measure the temperature of the hot elements before and after the installation of my designs, thus giving a quantitative measurement of their efficiency.

In order to reduce the thermal fluctuations on the fiber tips that are exposed to high optical power, I designed a collimator holder and an active thermal stabilization system for the fiber. The collimator holder is shown in figure 15(a); it is made from a block of aluminum and acts both as a heat sink and an ultra-stable holder for the collimator. The design features openings to access the focusing screw and locking screws of the collimator's lens, thus making it suitable for any collimator from the 60FC series of the SCHAFTER+KIRCHHOFF company. The thermal stabilization system makes use of a thermo-electric cooler (TEC) powered by a temperature controller to stabilize the temperature of the fiber up to 100 mK precision. The hot side of the TEC is mounted on a heat sink, whereas the cold side is attached to an aluminum clamp designed to match the shape of the fiber in order to maximize thermal contact and cooling efficiency. Inside this clamp is inserted a thermistor that measures the fiber temperature and sends it to the temperature controller. Thermal measurements of figure 15(a) show that the collimator holder dissipates the heat from the collimator and stays at room temperature while the temperature of the fiber is decreased by more than 10 °C after installing the system. As this last measurement was performed on a temporary setup, the optical fiber is not exactly matching the shape of the clamp. We can then affirm that the cooling efficiency will be optimized on the final experimental where the shape of the fiber is matching the design.

To protect the neighboring optics from the heat of the oven, I designed a thermal insulating box. This box can be seen in figure 15(b), it features 5 plates of 6 mm thick stainless steel and two optical windows. The steel plates are polished on the inside to reflect the incoming thermal radiation and sandblasted on the outside to protect the system from any unwanted specular reflections. The windows are V-coated for optimal transmission of both 1064 nm and 532 nm light. We can see on the thermal measurements of figure 15(b) that the outer surface of the oven reached more than 80 °C when used to heat the crystal at 214 °C. When the oven is mounted inside the insulating box and the temperature is stabilized, I measured the surface temperature of the outside and the top around 31 °C. The oven box design thus reduces the temperature of the outer surface by 50 °C but also protects the oven and the crystal from any surrounding dust and blocks any flow of hot air that could disturb the phase stability of the beam.
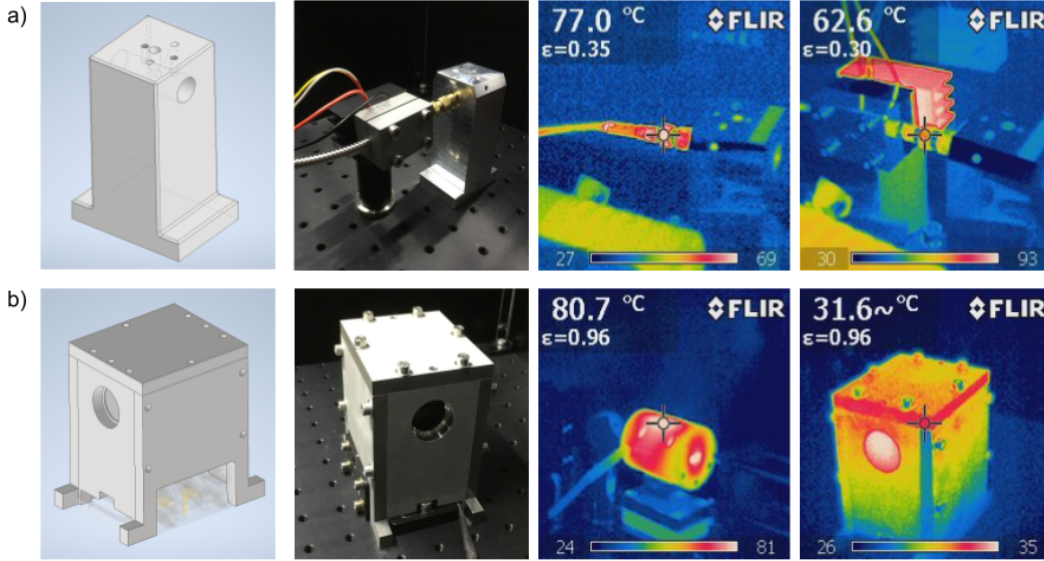
Figure 15: Thermal stabilization (a) and isolation (b) systems from computer-aided design to installation.

It is important to mention at this point that for surfaces with emissivity below 0.6, the measurement of temperature with an infrared camera can yield inaccurate results due to the important part of reflected radiation [32]. Shiny aluminum and brass exhibit emissivity below 0.3 meaning that the temperature measurements realized on the fiber and collimator holder are not extremely accurate. These results could be improved by measuring the temperature of a rough surface like tape directly in thermal contact with the element of interest.

3.2.2   Boyd-Kleinman analysis of SHG

Because SHG is a second-order nonlinear process, the intensity of the generated beam is proportional to the square of the intensity of the fundamental beam [33]. We could then think that better efficiency comes with strong focusing of the fundamental beam inside the crystal. On the other hand, a tight focus will lead to strong divergence of the beam and thus a rapid depletion of the intensity around the beam waist position. There is therefore a trade-off between strong focusing and long interaction length for each crystal length. In order to calculate the optimal focusing parameter, we integrate the power generated by infinitesimal slices of the crystal to obtain the total second-harmonic power: this is Boyd-Kleinman analysis [34] [35]. For a beam focused in the center of the crystal and neglected absorption losses, the integrated second harmonic power can be expressed from [36] as:

$$P_{SHG} = \frac{2\omega_1^2 d_{eff}^2 L_c k_1}{\pi \epsilon_0 c^3 n_1^2 n_2} \cdot P_1^2 \cdot h_{SHG}(\sigma, \xi, B)$$

where P_1 is the power of the fundamental wave, d_{eff} is the effective non-linear coefficient, n_1 and n_2 are the respective indices of refraction for the fundamental and second-harmonic laser beams, L_c is the crystal length, and k_1 is the fundamental wavevector. ϵ_0 and c are the vacuum permittivity and vacuum speed of light. Still according to [36], the general Boyd-Kleinman integral $h_{SHG}(\sigma, \xi, B)$ can be simplified to $h_{SHG}(\sigma, \xi)$ due to the absence of spatial beam walk-off in PPLN. We then obtain:

$$h_{SGH}(\sigma, \xi) = \frac{1}{4\xi} \left| \int_{-\xi}^{\xi} d\tau \frac{e^{i\sigma\tau}}{1 + i\tau} \right|^2$$

The parameter σ accounts for the phase-matching condition of the crystal, tunable with temperature. The dependency on the focusing of the beam is made through the parameter $\xi = L_c/b$ corresponding to the ratio of the crystal length and the confocal parameter $b = k_1 w_0^2$, where w_0 is the waist of the Gaussian beam. We know from [34] that the maximum value of h_{SHG} is 1.06. It is obtained when $\xi = 2.84$, corresponding in our case to a beam waist of 33 µm. However, according to section 2.1.2 we can calculate that with 10 W of IR power this would correspond to an intensity at the beam waist of 590 kW/cm² Because this value is above the damage threshold of MgO:PPLN (which is around 500 kW/cm²), we decided to focus the beam to a waist of 64 µm, thus reducing the intensity at the beam waist to 290 kW/cm² but at the same time reducing ξ to 1.4.
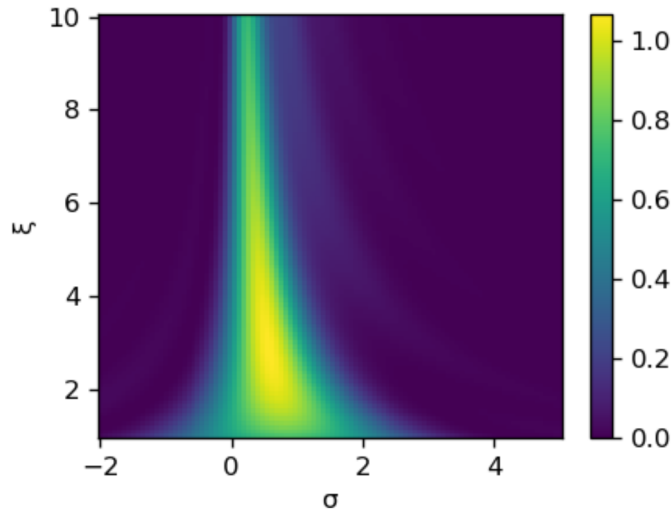

Figure 16: 2D plot of the Boyd-Kleinman integral depending on the phase-matching parameter σ and the focusing parameter ξ.

In figure 16 we show a 2D plot of the values of the simplified h_{SHG} depending on its two parameters. We observe that around the phase matching condition at $\sigma = 0.5$, h_{SHG} exhibits relatively slow variation with the focusing parameter ξ. We can then calculate that for ξ to 1.4 the Boyd-Kleinman integral's value is 0.92 and the theoretical SHG power should follow the relation:

$$P_{SHG} \ (in \ W) = 0.071 \cdot P_1^2 \ (in \ W^2)$$

3.3 Performance characterization

Before building the lattice setup, I had to make sure that the generated light was matching all the requirements of a lattice beam. The most important quantity is optical power because it defines the depth of each lattice site and the trap frequency as derived in section 2.1.3. Another crucial parameter is the beam shape. Indeed, in order to obtain efficient fiber coupling and to create a clean interference pattern in the lattice, the intensity distribution has to be the closest possible to a Gaussian distribution. The last important factor is intensity noise, i.e. the fluctuations of optical power in time. If the intensity fluctuates at a frequency matching the trap frequency or one of its multiples, parametric heating will occur and atoms in the lattice will be excited or even lost [37]. It is thus important to measure the amplitude of these fluctuations and to make sure they do not cause any threat to the stability of the lattice. I will present the characterization of these 3 quantities in the next subsections.

3.3.1 Influence of temperature and power on SHG efficiency

We know from section 2.2.5 that the quantum phase transition from a superfluid state to a Mott insulator state can occur for both species only for a lattice depth $V_{lat} > 16\,E_r$. If we aim at creating an optical lattice at $\lambda = 532$ nm with $N_{sites} = 10^6$ sites at a depth of $20\,E_r$ we would then need an optical power P_{SHG} of approximately 1.1 W according to 2.1.3.

In order to verify that the setup allows the generation of such a lattice, we now want to measure the maximum optical power P_{SHG} and the SHG efficiency defined as the ratio $\frac{P_{SHG}}{P_1}$. As seen in section 3.2.2, the efficiency should increase with the fundamental power P_1 but I decided to measure the efficiency only up to 12 W of input power in order to avoid damaging the crystal. The evolution of P_{SHG} for different input powers is given in figure 17(a). We can see that the power starts to increase with a quadratic dependency on P_1 until it reaches 4 W. We then observe a linear increase in P_1 followed by a saturation at around 10 W of IR. A maximum value of $P_{SHG} = 1.82$ W was obtained with 11.2 W of IR. The red curve in figure 17(b) is the corresponding SHG efficiency. It begins by behaving linearly as planned in theory, but we can see a peak at 19 % for $P_1 = 8.2$ W and then a decrease. This efficiency drop correlates with the saturation observed in the SHG power.

These values are compared in figure 17(a) to the theoretical values calculated from the Boyd-Kleinman analysis, showing that the experimental values are approximately two times smaller than the theory. This can be explained by the fact that Boyd-Kleinman analysis doesn't take into account the intensity depletion of the fundamental beam when generating green. In reality, the IR power is gradually transferred to the second harmonic thus reducing the efficiency over the range of the crystal. Also, we assumed that there are no absorption losses through our crystal. This is true for low optical power, but at high power a phenomenon called GReen Induced Infrared Absorption (GRIIRA) can occur [38]. At high green intensities, a Li ion can be knocked out of a lattice site and replaced by a Nb ion creating a polaron. This polaron can absorb IR light and will induce local heating or even damage the crystal. MgO doping of the crystal reduces the onset of GRIIRA because Mg ions can replace Nb ions, but it is still clearly visible in our setup. Indeed, as a result of local heating of the crystal we should see a decrease in the phase-matching
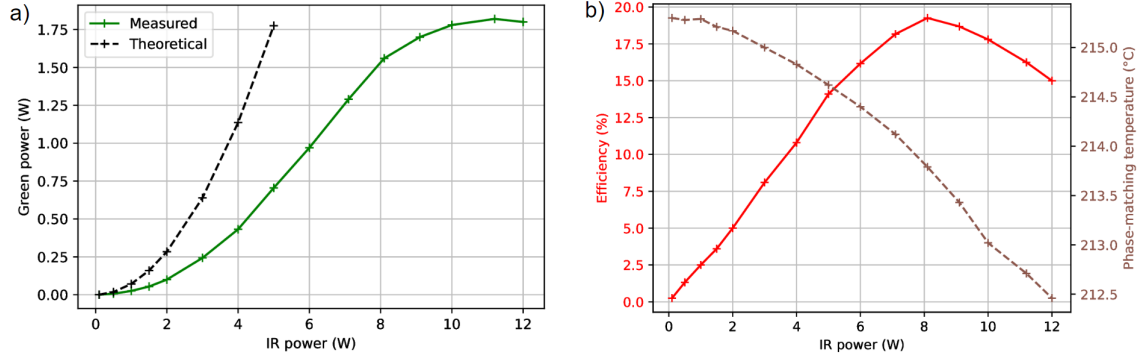
Figure 17: (a) Measured green power depending on the IR input power (green curve) compared to the theoretical analysis from section 3.2.2 (black dotted curve) (b) Evolution of SHG efficiency and phase-matching temperature with the input power.

temperature with respect to P_1, and that is exactly what I measured in 17(b). We can see on the brown curve that the phase-matching temperature decreases by more than 2.5 °C from its original value when P_1 increases. This temperature variation is approximately 25 times larger than the typical temperature acceptance bandwidth for this crystal length, proving that the phase-matching temperature was strongly shifted by GRIIRA. All these considerations could explain why the measured SHG power is lower than the theoretical calculation. Overall, the maximum value of $P_{SHG} = 1.82$ W is bigger than the 1.1 W required, it is thus sufficient to generate the desired lattice. The supplementary 720 mW allows us to compensate for the losses through the AOM, the optical fiber and the glass cell.

3.3.2 Beam quality

During SHG, the generated second harmonic beam is theoretically a Gaussian beam with the same confocal parameter b as the fundamental beam [34]. In our case, that would correspond to a beam diameter of 560 µm after collimation with a $f' = 75$ mm lens. In reality, high optical power inside the crystal will induce a photorefractive effect and can lead to beam distortions [39]. This is the reason why I originally obtained a beam diameter of 1.1 mm for the second harmonic beam. Because of this increase in size, an important part of the power was lost through the AOM that had an active aperture of 1 mm. I tackled this issue by replacing the lens with a $f' = 60$ mm lens to obtain a beam with a 900 µm diameter. I then used a CCD camera to measure the intensity profile of this beam at a position where it was slightly focused.

The beam profile is represented in figure 18(a) with the beam's intensity given in normalized units. In figure 18(b), a 2D Gaussian fit shows that the beam's intensity distribution corresponds indeed to a Gaussian profile. A quantitative measure of the Gaussian nature of the beam can be obtained by measuring the difference between the real intensity profile and the fit. This data is represented in figure 18(c) and attest that the beam profile does not diverge from a perfect Gaussian intensity distribution by values exceeding 10 % of its maximum intensity. This allows us to confirm that the beam can be fiber-coupled to the final experiment without too many losses (the measured coupling
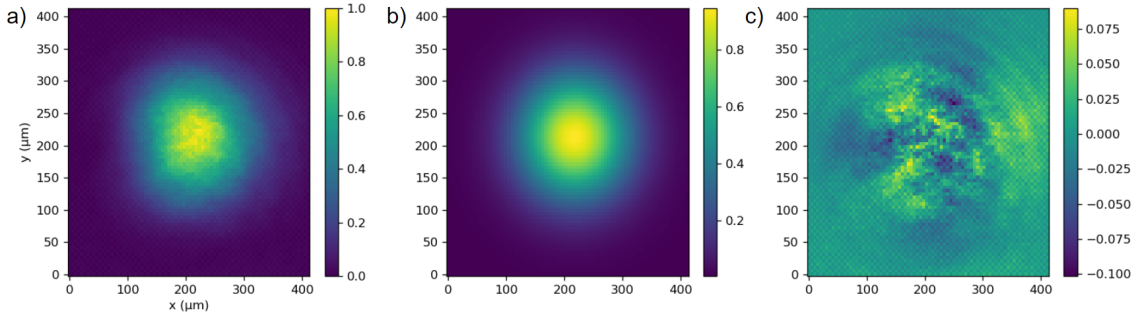
Figure 18: (a) Measured second harmonic beam profile, (b) 2D Gaussian fit of the data, (c) Optical aberrations resulting from the subtraction of the fit to the data.

efficiency is around 78 %) and that the lattice beam will generate a clean interference pattern.

3.3.3 Relative intensity noise

In an optical lattice, the lattice frequency ω_{lat} can usually range from 1 kHz to 100 kHz. If the intensity of the lattice beam fluctuates at a frequency close to ω_{lat} or one of its harmonics, a phenomenon called parametric heating will occur [37]. It can be seen as the transition of a trapped atom from the ground energy band to a higher band under the influence of intensity fluctuations. These excited atoms are ultimately heating the whole sample and can even escape from the trap. In order to make sure that parametric heating won't occur in the final lattice, we decided to measure the Relative Intensity Noise spectrum (RIN) of our green laser [40]. RIN quantifies the variation of intensity relative to a carrier signal and can be expressed in dBc/Hz with the formula :

$$RIN = 10 \cdot log \left(\frac{\langle \delta P^2 \rangle}{BW \cdot \overline{P}^2} \right)$$

with $\overline{P}$ the average optical power and $\langle \delta P^2 \rangle$ the temporal average of the squared power fluctuations over the measurement bandwidth BW. I measured the optical power by monitoring the voltage generated by a 125 MHz bandwidth photodiode. The DC voltage is related to $\overline{P}$ whereas the AC fluctuations are processed by a RHODE & SCHWARTZ 9 kHz - 6 GHz spectrum analyzer to deduce $\langle \delta P^2 \rangle$. RIN measurement was performed on 3 different signals: the incoming IR light at 8 W, the green light at 1.2 W after passing through the fiber, and the photodiode itself without any beam. Values are acquired from 10 kHz to 1 MHz with a resolution bandwidth of 1 kHz. The result is presented in figure 19(a). We can clearly see that the 3 curves overlap perfectly meaning that no intensity noise was measured above the noise of the photodiode. I also verified that this behavior is still present in the IR RIN for different values of the IR power, and obtained the same result with 5 W, 7 W and 10 W of IR. I first thought that the measurement was flawed, so I decided to artificially add noise to the laser intensity.

The Mephisto MOPA is designed with an integrated noise-reducing system called "Noise Eater". This function can be deactivated by the operator simply by pressing a button. I repeated the exact same RIN measurement with the "Noise Eater" turned off
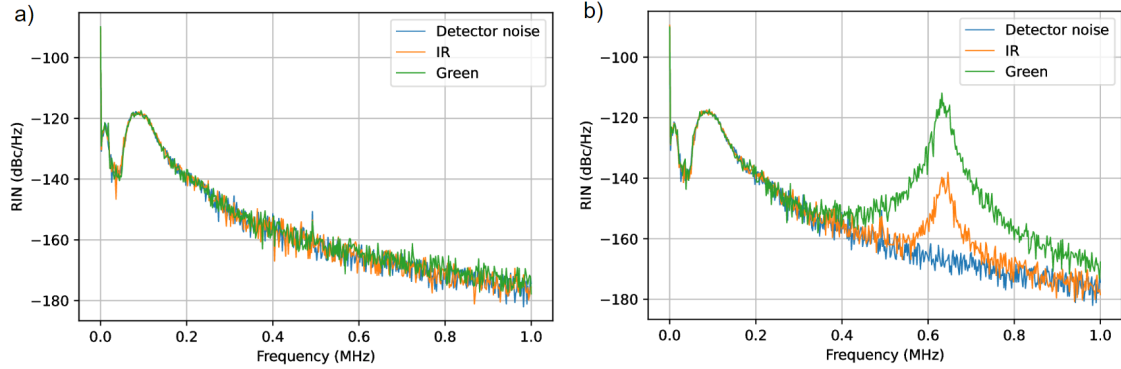
Figure 19: Relative intensity noise of the green light, the IR light and the detector with Noise Eater on (a) and off (b). Measurements were all realized with 1kHz resolution bandwidth.

and the result can be seen in figure 19(b). A peak of noise at -140 dBc/Hz appeared at 630 kHz in the RIN of the IR light. This peak is mainly due to relaxation oscillations in the laser's gain medium and is widely documented [41]. The presence of the same peak amplified by 20 dB after frequency doubling shows the transfer of the fundamental beam intensity noise to the green beam during the nonlinear process. The presence of this peak in the RIN measurement confirms that values acquired in 19(a) can actually be trusted and that there is no RIN above -120 dB in the green light over the span of 1MHz. We can use the definition of RIN to calculate that in the worst-case scenario (where RIN is -120 dB up to 1 MHz), intensity fluctuations would only go up to 0.01 %. This ensures that the lattice will be free of parametric heating.

4 Implementation of the lattice light on atoms

4.1 Optical lattice setup

With the green laser characterized, I was finally able to displace the second harmonic breadboard onto the experimental table. This table contains the oven, vacuum chamber, coils and laser beams allowing to cool Rb and Sr to quantum degeneracy. In order to align the green lattice beam, I overlapped it onto a previously built IR lattice. This IR lattice was already aligned on the position of the atoms ensuring a simple alignment of the green lattice beam. The lattice setup is shown in figure 20. Firstly, half-waveplates allow to control the direction of the polarization of the green light. Then, a dichroic mirror merges the green and IR beams. The beams are then focused through the vacuum chamber by an achromatic lens for $\lambda = 532$ nm and $\lambda = 1064$ nm. Angle and polarization are optimized in order to minimize the losses on the cell windows. The beams exiting the vacuum chamber on the other side are collimated by a second achromatic lens. They are then split by a dichroic mirror and retroreflected back onto their respective optical fiber. The retroreflected beams can be aligned precisely by optimizing the power of the light coupled back into the fibers.
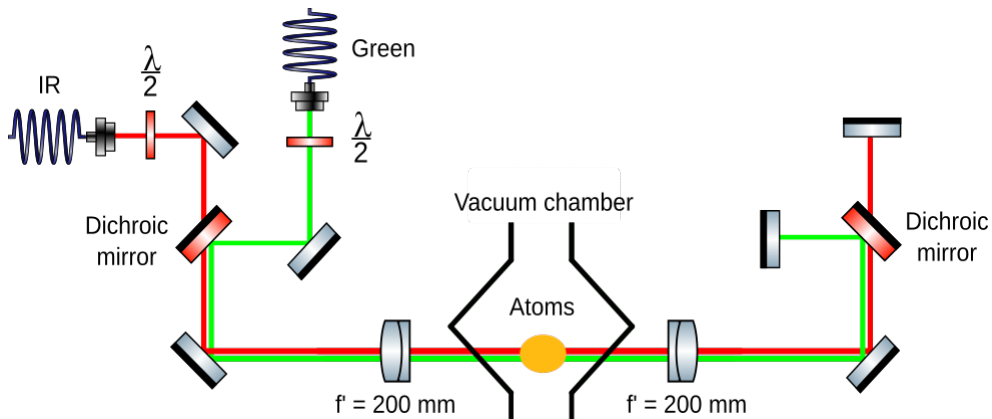

Figure 20: Optical lattice setup

In real optical lattices, losses can occur on the path of the retroreflected beam making it impossible to generate a perfect interference pattern. In this case, the lattice potential can be expressed from [42] as:

$$V(z) = \frac{V_{max}}{4} \cdot \left(1 + \rho^2 + 2\rho \cdot cos(2kz)\right)$$

with V_{max} the lattice depth for a system with no losses, and ρ the reflection coefficient defined as $\rho = P_{retro}/P_{input}$. Measurements on the setup gave a value of $P_{input} = 605$ mW and $\rho = 80.6\%$ resulting in a maximum lattice depth of $V_{lat} = 21.8 \ E_r$ for a cloud of Rb atoms.

4.2 Kapitza-Dirac diffraction

In order to optimize the lattice alignment and to measure precisely the lattice depth, we decided to perform a Kapitza-Dirac diffraction experiment on a Bose-Einstein condensate

(BEC) of Rb [43]. Kapitza-Dirac diffraction occurs when an optical lattice is adiabatically ramped up on a cloud of ultracold atoms. The atomic cloud is then diffracted into several orders similarly to the diffraction of light by a periodic structure, but with the roles of waves and matter reversed. The different diffraction orders correspond to quantum states with momenta of $2n \cdot \hbar k$ where n is a relative integer and k is the wavevector of the light. Atoms in these states can be seen as having experienced n times the absorption of a photon in one lattice direction followed by the stimulated emission of a photon in the opposite direction. This experiment is easier to perform on a BEC because of its superfluid nature allowing for a better separation of the different diffraction orders.

To observe Kapitza-Dirac diffraction, we image the atomic cloud with a time-of-flight measurement. First, we cool down Rb to create a nearly pure BEC, then we shine the lattice on the atoms for a duration τ and take a measurement. We then repeat the same sequence for a time 2τ and so on. Results of this experiment realized on a BEC of 35 000 atoms are shown in figure 21.
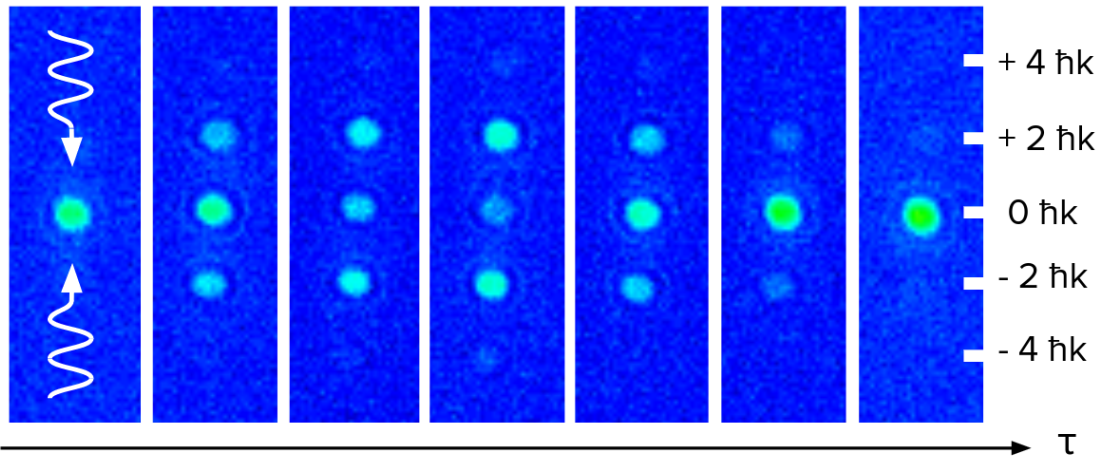

Figure 21: Kapitza-Dirac diffraction of a Rb Bose-Einstein condensate. The white arrows represent the direction of the lattice beams.

We can see that the BEC splits into several well-defined diffraction orders after applying the lattice pulse. Diffraction orders up to $\pm 4 \cdot \hbar k$ are visible. For longer pulses, the diffraction orders disappear and we observe a revival of the original BEC. We know that the frequency of this oscillation is exactly two times the lattice trap frequency ω_{lat}. Indeed, the adiabatic ramping of the lattice excites atoms from the fundamental band to the second excited band of the lattice. We can then measure precisely the trap frequency and the lattice depth by measuring the oscillation frequency of the diffraction experiment. We show this measurement in figure 22 by plotting the populations of the $0 \cdot \hbar k$ and $\pm 2 \cdot \hbar k$ orders for increasing duration of the lattice pulse. The population of each order is normalized to the total atom number in order to compensate for the loss of atoms happening during the experiment. Each set of data points is fitted with an exponentially decaying sinusoidal function. We can see that the diffraction and revival of the BEC can happen coherently more than 10 times in our experiment. A clear decrease in the oscillation amplitude is visible after several oscillations. This behavior is mainly caused by the decoherence
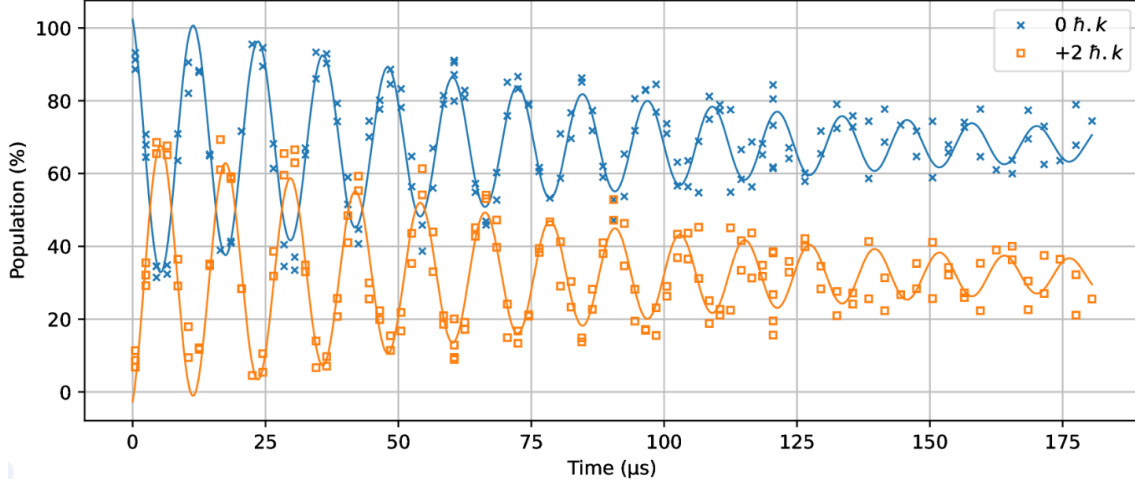
27

generated by collisions in the condensate.

Figure 22: Evolution of the normalized populations of the $0 \cdot \hbar k$ and $\pm 2 \cdot \hbar k$ orders for increasing duration of the lattice pulse. Each set of data points is fitted with an exponentially decaying sinusoidal function.

A fitting of the data gives an oscillation frequency of 82 ± 2 kHz corresponding to a lattice depth of 14 Er. This value is lower than the estimation realized in section 4.1, meaning that there is still room for improvement in the alignment of the lattice beams. However, this lattice depth is enough to allow for further studies on mixtures of Rb and Sr inside a green optical lattice.

5   Conclusion

Ultracold atoms and molecules in optical lattices constitute a relatively new and expanding field of modern physics. The great progress made during the last decades demonstrates the potential of these quantum systems to probe the fundamental properties of matter. The creation of ultracold open-shell molecules would open new possibilities for the simulation of complex many-body systems which are difficult or impossible to realize with conventional materials, such as the Haldane model [44] and the Harper-Hofstader model [45].

The work on the ultracold mixture of Rb and Sr in a $\lambda = 532$ nm optical lattice realized during my internship brings us one step closer to the creation of these molecules, but it also constitutes an interesting quantum system on its own. Thanks to a numerical simulation, the wavefunctions of atomic gases in optical lattices could be evaluated. The interaction between Rb and Sr atoms in the system was then proven to be sufficiently strong to be measured in the experiment with microwave clock spectroscopy. To this end, a high-power narrow-linewidth laser at $\lambda = 532$ nm was designed and built by generating the second harmonic of a $\lambda = 1064$ nm laser. It was demonstrated that the optical power of this laser is sufficient to allow the observation of the quantum phase transition from a superfluid to a Mott insulator for both Rb and Sr. Finally, relative intensity noise measurements proved that the laser light did not contain high-frequency noise that could induce parametric heating of the atoms in an optical lattice. Additional experiments will be done following the submission of this report. The intensity of the green laser will be actively stabilized, and the beam will be directed onto the atomic gases. Measurements of the lattice depth will be performed, and the band structure of the mixture of Rb and Sr will be probed if time allows it.

In parallel to the work presented in this report, I also took part in the characterization of a high-resolution microscope with long working distance. This microscope was recently built in the RbSr experiment and aims at optically addressing the atomic clouds of Rb and Sr with high resolution. It will allow the observation, excitation and manipulation of atoms in an optical lattice. My work on this project was to characterize the resolution of this microscope. I did not mention this work in the report, but I had the chance to share it via a poster presentation at the DPG Spring Meeting of the Atomic, Molecular, Quantum Optics and Photonics Section (SAMOP) at the University of Hannover in March 2023.

References

[1] W. D. Phillips and H. Metcalf, "Laser Deceleration of an Atomic Beam," *Physical Review Letters*, vol. 48, no. 9, pp. 596–599, Mar. 1982. [Online]. Available: https://link.aps.org/doi/10.1103/PhysRevLett.48.596

[2] E. L. Raab, M. Prentiss, A. Cable, S. Chu, and D. E. Pritchard, "Trapping of Neutral Sodium Atoms with Radiation Pressure," *Physical Review Letters*, vol. 59, no. 23, pp. 2631–2634, Dec. 1987. [Online]. Available: https://link.aps.org/doi/10.1103/PhysRevLett.59.2631

[3] R. Grimm, M. Weidemüller, and Y. B. Ovchinnikov, "Optical dipole traps for neutral atoms," 1999, publisher: arXiv Version Number: 1. [Online]. Available: https://arxiv.org/abs/physics/9902072

[4] W. Ketterle, "Nobel lecture: When atoms behave as waves: Bose-Einstein condensation and the atom laser," *Reviews of Modern Physics*, vol. 74, no. 4, pp. 1131–1151, Nov. 2002. [Online]. Available: https://link.aps.org/doi/10.1103/RevModPhys.74.1131

[5] M. Hachmann, Y. Kiefer, J. Riebesehl, R. Eichberger, and A. Hemmerich, "Quantum Degenerate Fermi Gas in an Orbital Optical Lattice," *Physical Review Letters*, vol. 127, no. 3, p. 033201, Jul. 2021. [Online]. Available: https://link.aps.org/doi/10.1103/PhysRevLett.127.033201

[6] H. A. Medicus, "Fifty years of matter waves," *Physics Today*, vol. 27, no. 2, pp. 38–45, Feb. 1974. [Online]. Available: http://physicstoday.scitation.org/doi/10.1063/1.3128444

[7] M. Greiner, O. Mandel, T. Esslinger, T. W. Hänsch, and I. Bloch, "Quantum phase transition from a superfluid to a Mott insulator in a gas of ultracold atoms," *Nature*, vol. 415, no. 6867, pp. 39–44, Jan. 2002. [Online]. Available: https://www.nature.com/articles/415039a

[8] T. H. Johnson, S. R. Clark, and D. Jaksch, "What is a quantum simulator?" *EPJ Quantum Technology*, vol. 1, no. 1, p. 10, Dec. 2014. [Online]. Available: http://www.epjquantumtechnology.com/content/1/1/10

[9] R. A. DiStasio, O. A. Von Lilienfeld, and A. Tkatchenko, "Collective many-body van der Waals interactions in molecular systems," *Proceedings of the National Academy of Sciences*, vol. 109, no. 37, pp. 14 791–14 795, Sep. 2012. [Online]. Available: https://pnas.org/doi/full/10.1073/pnas.1208121109

[10] E. A. Pazyuk, A. V. Zaitsevskii, A. V. Stolyarov, M. Tamanis, and R. Ferber, "Laser synthesis of ultracold alkali metal dimers: optimization and control," *Russian Chemical Reviews*, vol. 84, no. 10, pp. 1001–1020, Oct. 2015. [Online]. Available: https://iopscience.iop.org/article/10.1070/RCR4534

[11] V. Barbé, A. Ciamei, B. Pasquiou, L. Reichsöllner, F. Schreck, P. S. Żuchowski, and J. M. Hutson, "Observation of Feshbach resonances between alkali and closed-shell

atoms," *Nature Physics*, vol. 14, no. 9, pp. 881–884, Sep. 2018. [Online]. Available: https://www.nature.com/articles/s41567-018-0169-x

[12] K. Waiblinger, J. R. Williams, and J. P. D'Incao, "Quenched magneto-association of ultracold Feshbach molecules," *Physical Review A*, vol. 104, no. 3, p. 033310, Sep. 2021. [Online]. Available: https://link.aps.org/doi/10.1103/PhysRevA.104.033310

[13] I. Bloch, "Ultracold quantum gases in optical lattices," *Nature Physics*, vol. 1, no. 1, pp. 23–30, Oct. 2005. [Online]. Available: https://www.nature.com/articles/nphys138

[14] A. Lüscher and A. M. Läuchli, "Exact diagonalization study of the antiferromagnetic spin-1/2 Heisenberg model on the square lattice in a magnetic field," *Physical Review B*, vol. 79, no. 19, p. 195102, May 2009. [Online]. Available: https://link.aps.org/doi/10.1103/PhysRevB.79.195102

[15] A. Kox, "H.A. Lorentz, lectures on electron theory, first edition (1909)," in *Landmark Writings in Western Mathematics 1640-1940*. Elsevier, 2005, pp. 778–783. [Online]. Available: https://linkinghub.elsevier.com/retrieve/pii/B9780444508713501418

[16] A. Urech, I. H. A. Knottnerus, R. J. C. Spreeuw, and F. Schreck, "Narrow-line imaging of single strontium atoms in shallow optical tweezers," 2022, publisher: arXiv Version Number: 1. [Online]. Available: https://arxiv.org/abs/2202.05727

[17] S. Will, *From Atom Optics to Quantum Simulation: Interacting Bosons and Fermions in Three-Dimensional Optical Lattice Potentials*, ser. Springer Theses. Berlin, Heidelberg: Springer Berlin Heidelberg, 2013. [Online]. Available: https://link.springer.com/10.1007/978-3-642-33633-1

[18] G.-B. Jo, J. Guzman, C. K. Thomas, P. Hosur, A. Vishwanath, and D. M. Stamper-Kurn, "Ultracold Atoms in a Tunable Optical Kagome Lattice," *Physical Review Letters*, vol. 108, no. 4, p. 045305, Jan. 2012. [Online]. Available: https://link.aps.org/doi/10.1103/PhysRevLett.108.045305

[19] L. Su, A. Douglas, M. Szurek, R. Groth, S. F. Ozturk, A. Krahn, A. H. Hébert, G. A. Phelps, S. Ebadi, S. Dickerson, F. Ferlaino, O. Marković, and M. Greiner, "Dipolar quantum solids emerging in a Hubbard quantum simulator," 2023, publisher: arXiv Version Number: 1. [Online]. Available: https://arxiv.org/abs/2306.00888

[20] E. Haller, M. J. Mark, R. Hart, J. G. Danzl, L. Reichsöllner, V. Melezhik, P. Schmelcher, and H.-C. Nägerl, "Confinement-Induced Resonances in Low-Dimensional Quantum Systems," *Physical Review Letters*, vol. 104, no. 15, p. 153203, Apr. 2010. [Online]. Available: https://link.aps.org/doi/10.1103/PhysRevLett.104.153203

[21] P. Jessen and I. Deutsch, "Optical Lattices," in *Advances In Atomic, Molecular, and Optical Physics*. Elsevier, 1996, vol. 37, pp. 95–138. [Online]. Available: https://linkinghub.elsevier.com/retrieve/pii/S1049250X08600993

[22] G. H. Wannier, "The Structure of Electronic Excitation Levels in Insulating Crystals," *Physical Review*, vol. 52, no. 3, pp. 191–197, Aug. 1937. [Online]. Available: https://link.aps.org/doi/10.1103/PhysRev.52.191

[23] D. P. Arovas, E. Berg, S. A. Kivelson, and S. Raghu, "The Hubbard Model," *Annual Review of Condensed Matter Physics*, vol. 13, no. 1, pp. 239–274, Mar. 2022. [Online]. Available: https://www.annualreviews.org/doi/10.1146/annurev-conmatphys-031620-102024

[24] D. Jaksch, "Bose-Einstein condensation and applications," Ph.D. dissertation, 1999, bibliographic information available from INIS: http://inis.iaea.org/search/search.aspx?orig_q=RN:34000013; Available from Univ. Bibliothek Innsbruck, Innrain 50, 6010 Innsbruck (AT). [Online]. Available: http://inis.iaea.org/search/search.aspx?orig_q=RN:34000013

[25] P. Phillips, "Mottness," *Annals of Physics*, vol. 321, no. 7, pp. 1634–1650, Jul. 2006. [Online]. Available: https://linkinghub.elsevier.com/retrieve/pii/S0003491606000765

[26] A. Ciamei, J. Szczepkowski, A. Bayerle, V. Barbé, L. Reichsöllner, S. M. Tzanova, C.-C. Chen, B. Pasquiou, A. Grochola, P. Kowalczyk, W. Jastrzebski, and F. Schreck, "The RbSr ^{2} Sigma $^+$ ground state investigated *via* spectroscopy of hot and ultracold molecules," *Physical Chemistry Chemical Physics*, vol. 20, no. 41, pp. 26 221–26 240, 2018. [Online]. Available: http://xlink.rsc.org/?DOI=C8CP03919D

[27] J. P. D'Incao and B. D. Esry, "Ultracold Three-Body Collisions near Overlapping Feshbach Resonances," *Physical Review Letters*, vol. 103, no. 8, p. 083202, Aug. 2009. [Online]. Available: https://link.aps.org/doi/10.1103/PhysRevLett.103.083202

[28] T. Chalopin, "Optical superlattices in quantum gas microscopy," *Nature Reviews Physics*, vol. 3, no. 9, pp. 605–605, Jul. 2021. [Online]. Available: https://www.nature.com/articles/s42254-021-00357-8

[29] K. I. Martin, W. A. Clarkson, and D. C. Hanna, "Stable, high-power, single-frequency generation at 532 nm from a diode-bar-pumped Nd:YAG ring laser with an intracavity LBO frequency doubler," *Applied Optics*, vol. 36, no. 18, p. 4149, Jun. 1997. [Online]. Available: https://opg.optica.org/abstract.cfm?URI=ao-36-18-4149

[30] J. A. Armstrong, N. Bloembergen, J. Ducuing, and P. S. Pershan, "Interactions between Light Waves in a Nonlinear Dielectric," *Physical Review*, vol. 127, no. 6, pp. 1918–1939, Sep. 1962. [Online]. Available: https://link.aps.org/doi/10.1103/PhysRev.127.1918

[31] M. Houe and P. D. Townsend, "An introduction to methods of periodic poling for second-harmonic generation," *Journal of Physics D: Applied Physics*, vol. 28, no. 9, pp. 1747–1763, Sep. 1995. [Online]. Available: https://iopscience.iop.org/article/10.1088/0022-3727/28/9/001

[32] M. Planck, "Ueber das Gesetz der Energieverteilung im Normalspectrum," *Annalen der Physik*, vol. 309, no. 3, pp. 553–563, 1901. [Online]. Available: https://onlinelibrary.wiley.com/doi/10.1002/andp.19013090310

[33] R. W. Boyd, "The Nonlinear Optical Susceptibility," in *Nonlinear Optics.* Elsevier, 2008, pp. 1–67. [Online]. Available: https://linkinghub.elsevier.com/retrieve/pii/B9780123694706000010

[34] G. D. Boyd and D. A. Kleinman, "Parametric Interaction of Focused Gaussian Light Beams," *Journal of Applied Physics*, vol. 39, no. 8, pp. 3597–3639, Jul. 1968. [Online]. Available: https://pubs.aip.org/aip/jap/article/39/8/3597-3639/5204

[35] D. A. Kleinman, A. Ashkin, and G. D. Boyd, "Second-Harmonic Generation of Light by Focused Laser Beams," *Physical Review*, vol. 145, no. 1, pp. 338–379, May 1966. [Online]. Available: https://link.aps.org/doi/10.1103/PhysRev.145.338

[36] J. R. Daniel, S.-W. Tsai, and B. Hemmerling, "Analytical Approximation of the Second-Harmonic Conversion Efficiency," 2020, publisher: arXiv Version Number: 1. [Online]. Available: https://arxiv.org/abs/2009.08430

[37] T. Boulier, J. Maslek, M. Bukov, C. Bracamontes, E. Magnan, S. Lellouch, E. Demler, N. Goldman, and J. Porto, "Parametric Heating in a 2D Periodically Driven Bosonic System: Beyond the Weakly Interacting Regime," *Physical Review X*, vol. 9, no. 1, p. 011047, Mar. 2019. [Online]. Available: https://link.aps.org/doi/10.1103/PhysRevX.9.011047

[38] Y. Furukawa, K. Kitamura, A. Alexandrovski, R. K. Route, M. M. Fejer, and G. Foulon, "Green-induced infrared absorption in MgO doped LiNbO3," *Applied Physics Letters*, vol. 78, no. 14, pp. 1970–1972, Apr. 2001. [Online]. Available: https://pubs.aip.org/aip/apl/article/78/14/1970-1972/517086

[39] C. Gu and P. Yeh, "Photorefractive materials, effects, and applications," V. L. Brudny, S. A. Ledesma, and M. C. Marconi, Eds., Tandil, Argentina, Aug. 2001, pp. 9–13. [Online]. Available: http://proceedings.spiedigitallibrary.org/proceeding.aspx?articleid=885740

[40] R. Paschotta, "Noise in Laser Technology: Part 1: Intensity and Phase Noise," *Optik & Photonik*, vol. 4, no. 2, pp. 48–50, Jun. 2009. [Online]. Available: https://onlinelibrary.wiley.com/doi/10.1002/opph.201190028

[41] A. Schlatter, S. C. Zeller, R. Grange, R. Paschotta, and U. Keller, "Pulse-energy dynamics of passively mode-locked solid-state lasers above the Q-switching threshold," *Journal of the Optical Society of America B*, vol. 21, no. 8, p. 1469, Aug. 2004. [Online]. Available: https://opg.optica.org/abstract.cfm?URI=josab-21-8-1469

[42] S. Will, "Interacting bosons and fermions in three-dimensional optical lattice potentials," Ph.D. dissertation, Johannes Gutenberg-Universität Mainz, 2011. [Online]. Available: https://openscience.ub.uni-mainz.de/handle/20.500.12030/2149

[43] D. L. Freimund, K. Aflatooni, and H. Batelaan, "Observation of the Kapitza–Dirac effect," *Nature*, vol. 413, no. 6852, pp. 142–143, Sep. 2001. [Online]. Available: https://www.nature.com/articles/35093065

[44] Q.-Y. Liang, D. Trypogeorgos, A. Valdés-Curiel, J. Tao, M. Zhao, and I. B. Spielman, "Coherence and decoherence in the Harper-Hofstadter model," *Physical Review Research*, vol. 3, no. 2, p. 023058, Apr. 2021. [Online]. Available: https://link.aps.org/doi/10.1103/PhysRevResearch.3.023058

[45] G. Jotzu, M. Messer, R. Desbuquois, M. Lebrat, T. Uehlinger, D. Greif, and T. Esslinger, "Experimental realization of the topological Haldane model with ultracold fermions," *Nature*, vol. 515, no. 7526, pp. 237–240, Nov. 2014. [Online]. Available: https://www.nature.com/articles/nature13915